View metadata, citation and similar papers at core.ac.uk

brought to you by CORE

provided by Archivio istituzionale della ricerca - Politecnico di Milano

Nanoscale

ARTICLE

Highly Active Nickel-Cobalt/Nanocarbon Thin Films as Efficient Water Splitting Electrodes

Received 00th January 20xx,
Accepted 00th January 20xx

DOI: 10.1039/x0xx00000x

www.rsc.org/

Bita Bayatsarmadi,[a] Yao Zheng,[a] Valeria Russo,[b] Lei Ge[c], Carlo Spartaco Casari,[b,*] and Shi-Zhang Qiao[a,*]

Developing low cost, highly active and stable electrocatalysts for both the hydrogen evolution reaction (HER) and the oxygen evolution reaction (OER) using the same electrolyte has remained a major challenge. Herein, we report a novel and robust material comprised of Nickel-Cobalt nanoparticles coated on a porous nitrogen-doped carbon (NC) thin film synthesized via a two-step pulsed laser deposition technique. The optimized sample ($Ni_{0.5}Co_{0.5}$/NC) achieved lowest overpotentials of 176 mV and 300 mV at a current density of 10 $mAcm^{-2}$ for HER and OER, respectively. The optimized OER activity might be attributed to the available metal oxide nanoparticles with effective electronic structure configuration and enhanced mass/charge transport capability. At the same time, the porous nitrogen doped carbon incorporated with cobalt and nickel species can serve as an excellent HER catalyst. As a result, the newly developed electrocatalysts manifest high current densities and strong electrochemical stability in overall water splitting, outperforming most of the previously reported non-precious metal-based catalysts.

Introduction

In combatting global warming, development of renewable energy systems, and in particular energy storage, is vital in order to reduce society's dependence on the finite fossil fuels. Hence, it is essential to develop efficient, low-cost and safe energy storage devices for powering vehicles and electronic devices.[1, 2] Electrochemical water splitting represents one of the most important methods for renewable energy storage by generating hydrogen fuel.[3-5] In electrocatalytic water splitting, both water reduction and oxidation reactions are constrained by sluggish kinetics. Currently, the state-of-the-art catalysts used to split water are noble metal-based catalysts including Pt/C and IrO_2/C for the hydrogen evolution reaction (HER) and the oxygen evolution reaction (OER), respectively. These materials, however, are expensive, scarce and suffer low stability.[6, 7] Thus, inexpensive and durable non-noble metal electrocatalysts, such as non-precious metal[8], metal composite[9] and metal-free nanostructures[10], as well as their hybrids[11], have received much attention recently. First row transition metal-based materials have had a particular interest and have been intensively investigated as potential candidates for water splitting electrocatalysts.

Recent developments demonstrate that the catalytic activity of non-precious metal-based catalysts can be substantially tuned by the doping or fabrication of binary metallic mixtures.[12, 13] Several strategies have been reported to further improve the catalytic activity of the aforementioned catalysts such as: creating porosity within the structure, immobilizing nanoparticles on carbon supports to increase the surface area and available active sites and making multi-metallic catalysts due to the synergistic interactions between different metals.[14-16] This enhancement may involve morphology changes and/or chemical changes with the possibility of creating bimetallic active sites with carbon bridging.

On the other hand, catalysts in large scale applications need to deliver high current density with low overpotential and high stability and durability.[17] Currently, most of the reported transition metal-based catalysts are powders which need to be coated on a conductive substrate (e.g. glassy carbon electrodes) with the help of polymeric binders (e.g. Nafion). This may result in a decrease in contact area between the electrolyte and catalytic active sites and poor stability (i.e. peeling off from the substrate) causing loss in electrocatalytic performance.[18] Pulsed laser deposition (PLD) is a versatile synthesis technique to finely control the structure and property of synthesized materials. PLD provides several advantages compared to other techniques including deposition of thin films with either porous/hierarchical structure or smooth surface in which their chemical compositions are quite close to that of the target, even for multicomponent targets as shown in the case of nanostructured doped oxides for energy applications.[19-21] In addition, PLD can be used to fabricate transition-metal based nanoparticles supported on surfaces[22, 23] including conductive supports to be directly utilized as an electrode for both HER and OER reactions.[24]

[a] School of Chemical Engineering, University of Adelaide, Adelaide, SA 5005, Australia. Email: s.qiao@adelaide.edu.au
[b] Department of Energy, Politecnico di Milano, via Ponzio 34/3, 20133 Milano, Italy. Email: carlo.casari@polimi.it
[c] School of Chemical Engineering, University of Queensland, Brisbane, QLD 4072, Ausralia

Electronic Supplementary Information (ESI) available: [details of any supplementary information available should be included here]. See DOI: 10.1039/x0xx00000x

This journal is © The Royal Society of Chemistry 20xx

Please do not adjust margins

Please do not adjust margins

However, pairing the two electrode reactions for practical use is difficult due to the activity and stability issues at different pH ranges. Therefore, developing a bifunctional electrocatalyst with high activity towards both OER and HER in the same electrolyte becomes important yet challenging.

Herein, we report a porous carbon film coated with Nickel-Cobalt nanoparticles via a two-step PLD process at room temperature in which nitrogen dopants are incorporated into the carbon framework by ablation under reactive and highly pure nitrogen gas (designated as Ni_xCo_{1-x}/NC). The obtained hybrids directly served as a binder- and conductive-agent-free electrode and exhibited good electrocatalytic performances toward both HER and OER. The sample with optimized Ni-Co molar ratio ($Ni_{0.5}Co_{0.5}$/NC) achieved the lowest overpotentials of 176 mV and 300 mV at a current density of 10 $mAcm^{-2}$ toward the HER and OER, respectively. This electrode was also applied as a bifunctional electrocatalyst for a two-electrode water splitting cell which could achieve a current density of 10 $mAcm^{-2}$ at a low voltage of 1.75 V, which is lower than that of individual metallic electrodes (Ni/NC and Co/NC). Our results show great promise in developing new families of non-precious metal-based bifunctional electrocatalysts using controlled conversion of homogeneous metal complexes into solid-state carbon catalysts.

Experimental

Material synthesis

Targets and substrate preparation: High purity (99.99%) graphite, ultra-high purity nickel foil (2.5 mm thick) and a cobalt target were used for deposition of Nickel-Cobalt/N-carbon. Silicon wafer and copper foils (1 cm × 1 cm pieces) were used as substrates for films deposition. All the substrates were cleaned by sonication in isopropanol for 20 minutes, rinsing in isopropanol and drying using a nitrogen gas flow before deposition.

Synthesis of N-doped carbon film: The porous nitrogen-doped carbon films were deposited at room temperature by reactive PLD using a Nd:YAG pulsed laser (λ = 532 nm, duration of 9 ns and repetition rate of 10 Hz) with a pulse energy of 200 mJ. The beam was directed onto a rotating graphite target with a 45° angle of incidence. Laser pulses ablated the target ejecting material in a plasma plume. Ablated species were deposited on the substrates to form the carbon thin film. The ablation process was performed in the presence of nitrogen as background gas to tune morphology, structure and composition of the deposited film. The distance between the target and the substrates and the laser spot size on the target were kept at 5 cm and 12.5 mm^2, respectively. The chamber was first evacuated to a base pressure (10^{-3} Pa) using a primary scroll pump and a turbo-molecular pump. Then, the chamber was fed with nitrogen gas (99.99% purity) at 50 Pa to introduce nitrogen into the carbon framework. The deposition time (i.e. number of laser pulses) was set to 120 seconds to form a film with the thickness of 250 nm. Mass loading measurements were obtained using a quartz crystal microbalance (QCM) and keeping other deposition conditions (i.e. chamber pressure, pulse energy, target to substrate (QCM in the case of mass loading measurements)) constant.

Synthesis of Nickel-Cobalt/N-carbon film: High purity Cobalt targets decorated with different Nickel strips (Fig. S1) were used as bimetallic targets for deposition of Ni_xCo_{1-x} and N-carbon films from the previous step (used as a substrate). All deposition conditions were kept similar to conditions mentioned previously. Ni_xCo_{1-x} were deposited at background gas pressures of 50 Pa and deposition times were calculated based on a desired cobalt mass percentage (10 at %). All calculations have been done based on mass loading records from a quartz crystal microbalance (QCM) under constant PLD conditions (both carbon and cobalt deposition mass loading).

Chemical characterization

The morphology of synthesized samples was characterized by scanning electron microscope (SEM, ZEISS Supra40) operating at 10 kV. Elemental mapping was conducted using energy dispersive X-ray spectroscopy (EDAX) detector attached on ZEISS Supra40 and EDS spectra collected from EDAX detector attached to the JEM-2100. Raman spectra were collected on LabRAM (Horiba Ltd) with 532 nm laser line. X-ray diffraction (XRD) patterns (10-60° in 2θ) were collected on an X-ray diffractometer at 40 kV and 15 mA using Co-Kα radiation (Miniflx-600, Rigaku). The X-ray photoelectron spectroscopy (XPS) analysis was conducted on an Axis Ultra spectrometer (Kratos Analytical Ltd.) with monochromated AlKα radiation (1486.6 eV) at ca. 5×10^{-9} Pa.

Electrochemical characterization

All electrochemical measurements were performed in a three-electrode glass cell on a 760 workstation (Pine Research Instruments, US). The as-synthesized hybrid films were directly used as working electrodes, platinum wire as the counter electrode and Ag/AgCl/KCl (4 M) as the reference electrode. A flow of N_2 was maintained over the electrolyte (1.0 M KOH) during the OER and HER electrochemical measurements to eliminate dissolved oxygen. All potentials were referenced to a reversible hydrogen electrode (RHE) using the equation below:

$E_{RHE}=E_{Ag/AgCl} + (0.059\times pH + 0.205)$

Linear sweep voltammograms (LSVs) were recorded at 5 mVs^{-1} to minimize the capacitive current. The working electrodes were scanned several times until stabilization before data collection commenced. The internal resistance of electrochemical cell was 5 Ω and all cyclic voltammetry (CV) and linear sweep voltammetry (LSV) data were corrected for the iR contribution within the cell.

The Tafel slope was calculated according to the Tafel equation as follows:

$\eta = b\log j + a$,

where η is overpotential (V); j is the current density (mA cm^{-2}); b is the Tafel slope (mV dec^{-1}).

Electrode durability was tested using chronoamperometric response which was conducted at -1.5 V (vs. Ag/AgCl) for HER and +0.8V (vs. Ag/AgCl) for OER electrodes.

The electrical double layer capacitances (C_{dl}, μF cm^{-2}) of the working electrodes were obtained from double-layer charging-discharging plots using CV in a small potential range of -0.8 to -0.75 V (vs. Ag/AgCl) and at scan rates ranging from 10 to 100 mVs^{-1}. The

 This journal is © The Royal Society of Chemistry 20xx

Please do not adjust margins

plots of current density ($mAcm^{-2}$) at -0.775 V (vs. Ag/AgCl) against the scan rate are nearly linear and the slopes are C_{dl} ($\mu F\ cm^{-2}$).

The water splitting system was fabricated using a two-electrode cell configuration by integrating $Ni_{0.5}Co_{0.5}$/NC bi-functional catalyst as the anode and cathode in 1.0 M KOH. Polarization curves were obtained using LSV with a scan rate of 5 mV s^{-1}. Long-term durability tests were performed at a constant potential of 1.6V. Ni/NC‖Ni/NC, Co/NC‖Co/NC and Pt/C‖IrO_2/C two electrode water splitting cells were also studied to draw comparisons. All data for the two electrode electrolyzer were recorded without iR compensation.

Results and discussion

The fabrication process of nitrogen doped carbon supported binary nickel-cobalt nanoparticles (Ni_xCo_{1-x} /NC; x denotes molar ratio) is illustrated in Fig. 1. Porous structured nitrogen-doped carbon films were prepared on silicon wafers and copper foils as a substrate by Pulsed laser deposition (PLD) technique under reactive background gas at room temperature (Fig. S1a). This procedure is modified from our previous report.[25] The resultant N-carbon film features unique advantages due to its porous structure and represents a favorable support with unique properties such as high electrical conductivity and enhanced electron transfer. Next, binary Ni_xCo_{1-x} nanoparticles were deposited on the N-carbon film using

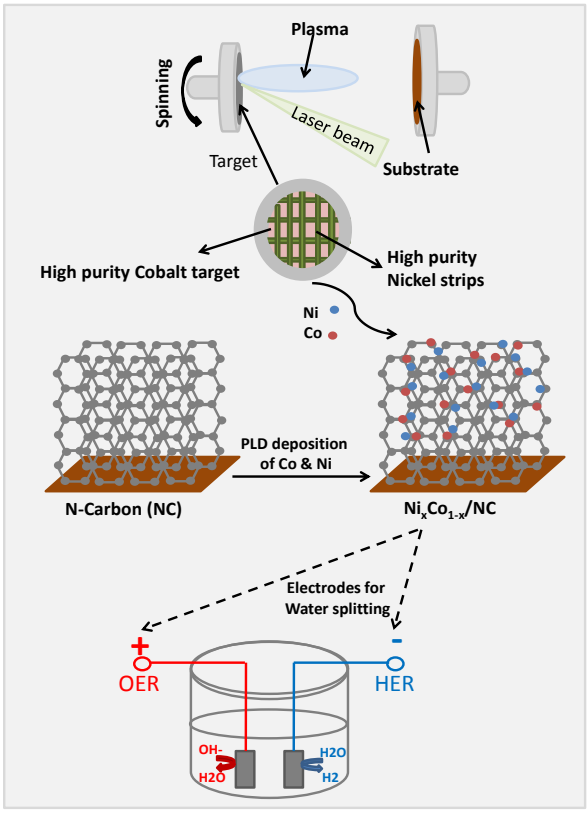

Fig. 1 Schematic illustration of the synthesis procedure of Ni_xCo_{1-x}/NC catalytic electrodes and their utilization in water splitting system.

designed bimetallic targets (Fig. S1b) and reactive PLD (λ = 532 nm with a pulse energy of 200 mJ) as described in the experimental section. Laser pulses ablated the spinning target ejecting material in a plasma plume. Ablated cobalt and nickel species were deposited on the substrates (N-Carbon) to form binary Ni_xCo_{1-x}/NC. The Ni/Co ratio was controlled by the number of nickel strips used at the designed target. The final products were directly utilized as electrodes for water splitting in concentrated alkaline electrolyte (1.0 M). To obtain some insights into the electrocatalytic activity relationship of binary Ni_xCo_{1-x}/NC, individual Ni/NC and Co/NC were prepared using the same method for comparison.

X-ray diffraction (XRD) was initially used to investigate the crystalline nature of the Ni_xCo_{1-x}/NC as shown in Fig. 2a. The XRD pattern demonstrates a broad peak centered around 19° and a diffraction peak at 26.3°, which suggests the availability of both amorphous and crystalline states of carbon, respectively. The broad peak corresponds to the disordered amorphous carbon[26] and the latter is attributed to the inter-plane (002) reflection of graphitic carbon which is related to the graphite-like stacking of the conjugated aromatic units[27, 28] with interlayer distance of 0.38 nm which is larger than that of graphite (0.34 nm) and similar to reported data[29, 30]. Moreover, diffraction peaks located at about 32°, 37°, 40°, 45°, 57° and 59° could be indexed to well-crystallized Ni-Co alloy which is bonded with either available O or N-C species.[31, 32] There are no additional diffraction peaks in the pattern attributed to individual Co and Ni, indicating the high phase purity of binary Ni-Co formed (Fig. S2).

The morphological and structural features of Ni_xCo_{1-x}/NC were examined by scanning electron microscopy (SEM). As shown in Fig. 2b, the relatively uniform structure and high porosity of the nanoporous N-carbon (acting as substrate) was maintained after deposition of binary Ni-Co species by tuning deposition parameters to prevent any morphology changes (Fig. S3). Fig. 2c shows the low magnification SEM cross-sectional image of the Ni_xCo_{1-x}/NC film followed by SEM energy dispersive X-ray spectroscopy (SEM-EDS) elemental mapping (Fig. 2d-g). The cross-sectional SEM image indicates the assembly of nanoparticles forming a thin film with a thickness of about 250 nm and a porous columnar nanostructure. The corresponding elemental mapping shows the presence of Ni, Co, C, and O in the thin film, verifying the uniform dispersion of these four elements. There is also no sign of ablated single species (Ni or Co) which can be clearly seen from the boundaries of the thin film from the corresponding elemental mapping images. It should be noted that nitrogen species are not detected due to the relatively small amount and the low spatial resolution of EDS elemental mapping. Thus, high-resolution transmission electron microscopy-EDS (TEM-EDS) spectrum was collected to confirm the presence of nitrogen species in the developed materials (Fig. S4).

Further, the surface chemistry of binary Ni_xCo_{1-x}/NC and individual Ni/NC and Co/NC electrodes were investigated by X-ray photoelectron spectroscopy (XPS). The XPS survey spectra (Fig. 3a) demonstrate the presence of C, N and O at all the prepared electrodes. Moreover, they confirm the presence of both Ni and Co species at Ni_xCo_{1-x}/NC while there is only Ni present in Ni/NC and Co present in Co/NC films. The molar ratio of Co and Ni in Ni_xCo_{1-x}/NC has been investigated by XPS and is summarized in Table S1. The

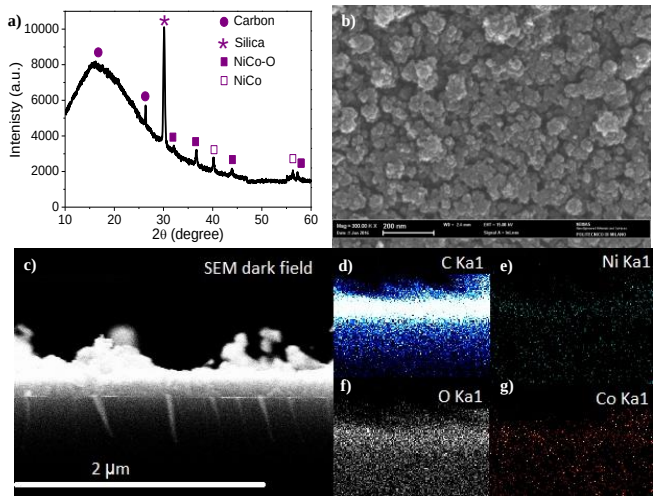

Fig. 2 (a) XRD spectrum (b) top view SEM image, (c) low-magnification cross-sectional SEM image (d-g) The corresponding SEM-EDS elemental mappings of C, O, Ni and Co of Ni_xCo_{1-x}/NC film.

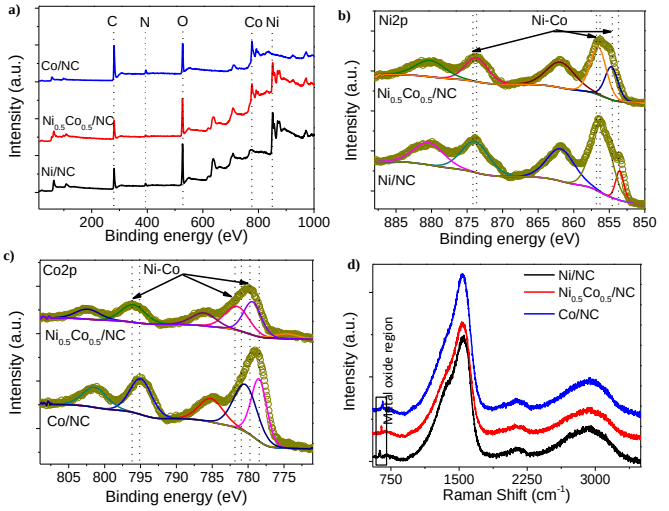

Fig. 3 (a) XPS survey of Ni/NC, $Ni_{0.5}Co_{0.5}$/NC and Co/NC films, (b) High-resolution Ni2p spectra of Ni/NC and $Ni_{0.5}Co_{0.5}$/NC, (c) High-resolution Co2p spectra of Co/NC and $Ni_{0.5}Co_{0.5}$/NC and (d) Raman Spectra of Ni/NC, $Ni_{0.5}Co_{0.5}$/NC and Co/NC films.

high-resolution Ni 2p spectrum of Ni_xCo_{1-x}/NC and Ni/NC are presented in Fig. 3b. For Ni/NC, two characteristic peaks at 856.3 eV and 873.1 eV, as well as the two satellite peaks at 861.8 and 880.7 eV, correspond well to Ni-O species.[33] Another peak at 852.7 eV might be attributed to the Ni bonded with available C-N species.[34] The Ni 2p XPS spectrum for Ni_xCo_{1-x}/NC represents all the five mentioned peaks with small shifts of about ±1 eV which could be assigned to the formation of Co-Ni alloys. Similarly, for Co elements in Co/NC, the $Co2p_{3/2}$ and $Co2p_{1/2}$ peaks at 781.3 and 795.5 eV as well as the two satellite peaks can be correlated to the presence of oxidized Co species (Fig. 3c).[35] There is also a peak assigned to metallic cobalt available at 778.2 eV which could be bonded with C-N species.[36] From Co 2p XPS spectrum of Ni_xCo_{1-x}/NC, the formation of Co-Ni alloy is further confirmed due to a small shift of 1eV for all five available peaks.[37]

Raman spectroscopy is able to provide structural information in carbon-based composite materials. Fig. 3d shows Raman spectra of the binary Ni_xCo_{1-x}/NC, exhibiting the typical fingerprint of amorphous carbon. In fact, the G and D modes, which are attributed to C-C stretching in the hexagonal plane of sp^2 carbon and to reduced size crystal domains and structural disorder, respectively, create a broad peak where the G band is the main contribution merged with D mode constituting a shoulder with an I_D/I_G intensity ratio of about 0.61 (Fig. S5 and Table S2).[38, 39] The weak band at about 2200 cm^{-1} is characteristic of the presence of a small fraction of sp- hybridized carbon[40-42] which might enhance the catalytic activity and selectivity of deposited materials due to high electron density coupled by restricted rotation of C-C bond.[43] The large band in the 2400-3200 cm^{-1} spectral region is the typical 2nd order Raman signal of amorphous carbon films. In addition, there is a weak peak at about 550-650 cm^{-1} assigned to the available metal oxides.[44, 45] In comparison to the individual Ni/NC and Co/NC, small shifts are observed in the vibrational bands and metal oxide active peaks of Ni_xCo_{1-x}/NC (Fig. S6 and Table S2). The small shifts of vibrational bands and metal oxide active peaks in binary Ni_xCo_{1-x}/NC indicate strong interaction/mixing between Co and Ni species as well as between the formed binary component and porous carbon nanosheets, which would be favorable for charge transport during electrochemical reactions.

The effective operation of electrocatalysts in concentrated electrolytes is a critical fig. of merit for practical applications.[46] Thus, with an average mass loading of 0.1 $mgcm^{-2}$ across all electrodes for both HER and OER, the electrocatalytic activity of Ni_xCo_{1-x}/NC (where x= 0.2, 0.3, 0.4, 0.5 and 0.7; measured by XPS), control samples (including Ni/NC and Co/NC), unsupported binary $Ni_{0.5}Co_{0.5}$, and benchmark samples (Pt/C or IrO_2/C) were evaluated in 1.0 M KOH solution using a typical three-electrode system. Since as-measured reaction currents cannot directly reflect the intrinsic behavior of catalysts due to the effect of ohmic resistance, an iR correction was applied to all of the initial data for further analysis. Fig. 4a shows HER linear sweep voltammetry (LSV) curves with a scan rate of 5 mV s^{-1}. For Ni_xCo_{1-x}/NC, an optimal HER catalytic activity was obtained when x=0.5 with the lowest onset potential (η_0 defined as the potential to reach 1 $mAcm^{-2}$) of 0.048 V and achieves the largest current density of 100 mA cm^{-2} at an overpotential of 0.363 V. Increasing or decreasing the Ni doping ratio (from x = 0.5) led to lower activities of the Ni_xCo_{1-x}/NC hybrid catalysts. Thus, the operating potentials to drive a cathodic current density of 10 $mAcm^{-2}$ (η_{10}) for $Ni_{0.5}Co_{0.5}$/NC and control samples were compared, which is related to the catalytic activity (Fig. 4b). As expected, Pt/C exhibits excellent activity with negligible overpotential (0.069 V) to deliver a current density of 10 $mAcm^{-2}$. Moreover, $Ni_{0.5}Co_{0.5}$/NC also shows a lower η_{10} of 0.176 V than other samples such as unsupported $Ni_{0.5}$ $Co_{0.5}$ (0.282 V), Ni/NC (0.406 V) and Co/NC (0.378 V). The overpotential of $Ni_{0.5}Co_{0.5}$/NC suggests its superior catalytic activity towards HER compared to other synthesized samples in this work and most earth-abundant, non-noble-metal HER catalysts in alkaline media (Table S3).

The HER kinetics of the prepared electrodes were studied by analyzing the Tafel plots which are recorded with the linear portions at low overpotential fitted to the Tafel equation (Fig. 4c and Fig. S7). A Tafel slope of 132.1 mV dec^{-1} for $Ni_{0.5}Co_{0.5}$/NC is larger than Pt/C (80.2 mV dec^{-1}), but is smaller than those of Ni/NC

This journal is © The Royal Society of Chemistry 20xx

Please do not adjust margins

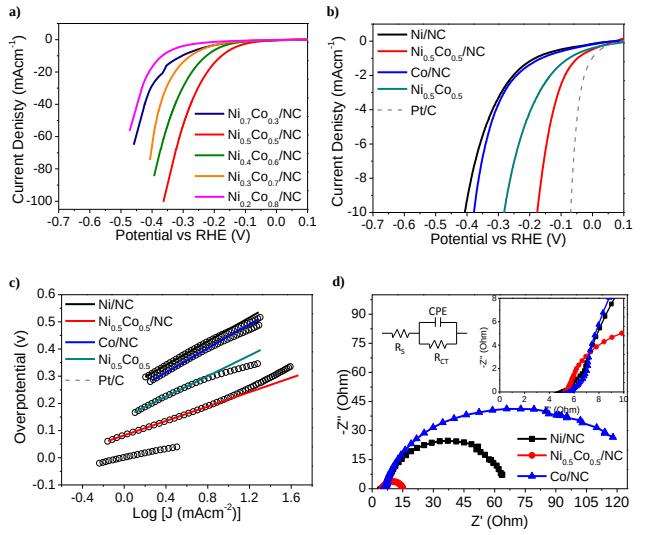

Fig. 4 (a) HER polarization curves of binary Ni_xCo_{1-x}/NC, (b) HER polarization curves and (c) Corresponding HER Tafel plots of Ni/NC, $Ni_{0.5}Co_{0.5}$/NC, Co/NC, unsupported $Ni_{0.5}Co_{0.5}$ and commercial Pt/C in 1.0 M KOH, (d) Nyquist plots of Ni/NC, Co/NC and $Ni_{0.5}Co_{0.5}$/NC at potential of -1.5 V (vs. Ag/AgCl) at 1.0M KOH.

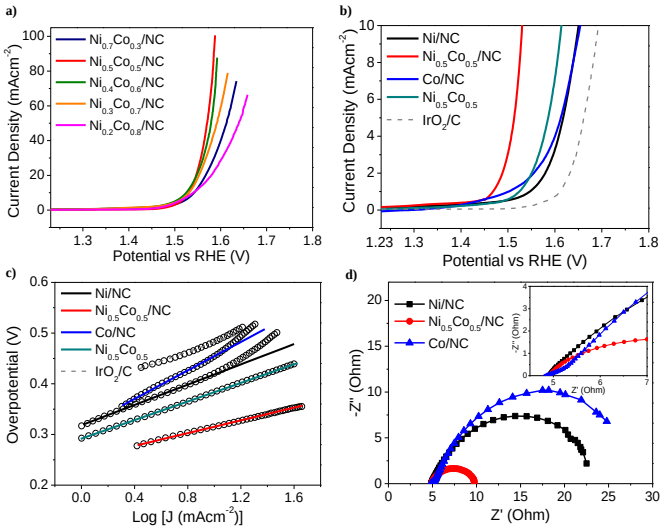

Fig. 5 (a) OER polarization curves of binary Ni_xCo_{1-x}/NC, (b) OER polarization curves and (c) Corresponding OER Tafel plots of Ni/NC, $Ni_{0.5}Co_{0.5}$/NC, Co/NC, unsupported $Ni_{0.5}Co_{0.5}$ and commercial IrO_2/C in 1.0 M KOH, (d) Nyquist plots of Ni/NC, Co/NC and $Ni_{0.5}Co_{0.5}$/NC at potential of +0.8 V (vs. Ag/AgCl) at 1.0M KOH.

(218.8 mV dec^{-1}), Co/NC (221.9 mV dec^{-1}) and unsupported $Ni_{0.5}Co_{0.5}$ (189.3 mV dec^{-1}), further confirming the favorable catalytic kinetic of $Ni_{0.5}Co_{0.5}$/NC for HER. On the basis of the Tafel analysis, the exchange current density of the $Ni_{0.5}Co_{0.5}$/NC catalyst was estimated to be 23.7 x 10^{-5} A cm^{-2}. This value is much higher than that reported for other non-precious metal-based catalysts.[47, 48]

Electrochemical impedance spectroscopy (EIS) tests were conducted to investigate the electrode kinetics under HER at an applied potential of -1.5 V (vs. Ag/AgCl) in 1.0 M alkaline solution. The semicircles in the Nyquist plot are attributed to the charge-transfer resistance (R_{CT}) and solution resistance (R_S), which are related to the electrocatalytic kinetics and a lower value corresponds to a faster reaction rate. Therefore, the EIS analysis confirmed a faster HER kinetic process on $Ni_{0.5}Co_{0.5}$/NC (R_{CT}= 10 Ω) than its individual components (Ni/NC and Co/NC) and other Ni_xCo_{1-x}/NC films which is consistent with its lower overpotential (Fig. 4d and S8).[49] Since electrode durability in concentrated alkaline solutions is very critical to evaluate catalyst performance, a long-term (60000 seconds) chronoamperometric test was also performed at a constant potential of -1.5V (vs. Ag/AgCl) for the $Ni_{0.5}Co_{0.5}$/NC electrode in 1.0 M KOH electrolyte. As shown in Fig. S9, 89% of the electrode activity is retained after long-term stability testing which can be attributed to the metal species embedded in the N-carbon framework.

The catalytic ability of Ni_xCo_{1-x}/NC to OER was also assessed in 1.0 M KOH solution. In typical LSV plots, the anodic current of all samples simultaneously increases as the potential becomes more positive, which is commonly observed for OER catalysts in alkaline media.[50] As shown in Fig. 5a and b, $Ni_{0.5}Co_{0.5}$/NC exhibited the lowest onset potential (η_0) of 1.467 V (vs RHE) and manifested a current density of 100 mA cm^{-2} at an overpotential as low as 0.358 V, indicative of the lowest energy input for driving OER among other binary counterparts, individual components (Ni/NC and Co/NC) and benchmark IrO_2/C. $Ni_{0.5}Co_{0.5}$/NC also shows a lower overpotential (0.300 V) to deliver a current density of 10 mA cm^{-2} when compared with other samples such as IrO_2/C (0.463 V), Ni/NC (0.420 V), Co/NC (0.430 V) and unsupported $Ni_{0.5}Co_{0.5}$ (0.380 V). Remarkably, the OER current of $Ni_{0.5}Co_{0.5}$/NC exceeds that of IrO_2/C throughout the whole potential range, indicating it has much better catalytic activity compared to this benchmark.

Tafel slopes and exchange current densities of all prepared electrodes were obtained from Tafel plots and the results are summarized in Fig. 5c, S10 and Table S4. As can be seen, the Tafel slopes for all the binary electrodes (Ni_xCo_{1-x}/NC) were around 62-80 mV dec^{-1}, which is in good agreement with the literature.[51, 52] $Ni_{0.5}Co_{0.5}$/NC confirms a higher OER activity compared to IrO_2/C (91.4 mV dec^{-1}), individual components (100.0 mV dec^{-1} and 136.2 mV dec^{-1} for Ni/NC and Co/NC, respectively) and unsupported $Ni_{0.5}Co_{0.5}$ (91.6 mV dec^{-1}). The exchange current densities were calculated to be 9.8 x 10^{-5}, 2.6 x 10^{-5}, 8.7 x 10^{-6} and 6.5 x 10^{-5} Acm^{-2} for $Ni_{0.5}Co_{0.5}$/NC, Ni/NC, Co/NC and unsupported $Ni_{0.5}Co_{0.5}$, respectively, implying the superior OER catalytic performance of $Ni_{0.5}Co_{0.5}$/NC.

As shown in Fig. 5d, the Nyquist plot of $Ni_{0.5}Co_{0.5}$/NC demonstrates a semicircle which is an indication of the charge transfer residence of the electrode. The calculated resistance of $Ni_{0.5}Co_{0.5}$/NC (4.9 Ω) is significantly less than that of individual Ni/NC (>15 Ω) and Co/NC (>20 Ω) electrodes which might be attributed to the higher OER activity. Additionally, long-term stability testing shows a seldom attenuation in current density at 0.8 V versus Ag/AgCl (Fig. S11).

As for the role of the Ni ion in the electrocatalytic activity of the prepared electrodes, the difference of HER and OER metrics (relative potential at E = -5 $mAcm^{-2}$ from the HER polarization curve and relative potential at E = 10 $mAcm^{-2}$ from the OER polarization curve; $\Delta E_{Overall} = E_{j=-5} - E_{j=10}$) obtained using single Ni/NC, Co/NC and binary Ni_xCo_{1-x}/NC catalysts as a water-splitting electrode were

Please do not adjust margins

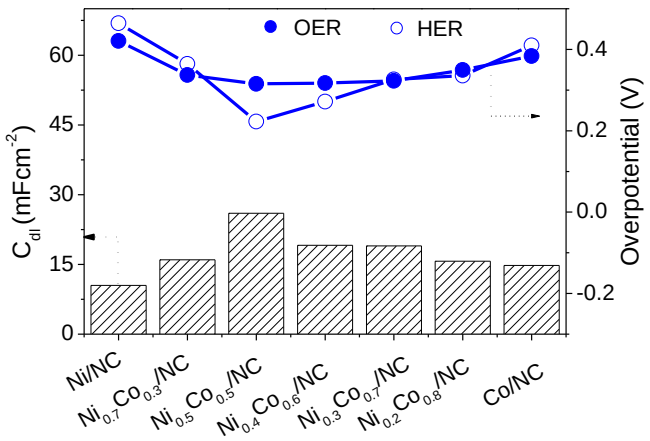

Fig. 6 Roughness factor and HER/OER overpotential to reach a current density of 10 mAcm^{-2} plots of binary Ni_xCo_{1-x}/NC and individual Ni/NC and Co/NC.

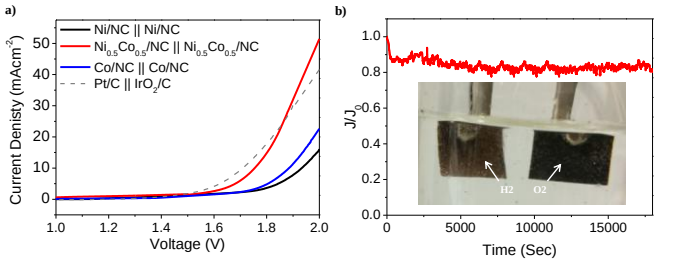

Fig. 7 (a) LSV plots of water splitting at Ni/NC‖Ni/NC, $Ni_{0.5}Co_{0.5}$/NC‖$Ni_{0.5}Co_{0.5}$/NC, Co/NC‖Co/NC and Pt/C‖IrO_2/C as cathode and anode electrodes and (b) Chronoamperometric response of $Ni_{0.5}Co_{0.5}$/NC‖$Ni_{0.5}Co_{0.5}$/NC cell working for splitting water at a voltage of 1.5 V for 18000 seconds.

compared (Fig. S12). The smaller ΔE is, the closer the catalyst is to an ideal bifunctional water-splitting electrode. Remarkably, binary $Ni_{0.5}Co_{0.5}$/NC can yield smaller ΔE (1.705 V) than single Ni/NC and Co/NC (2.057 and 2.032 V, respectively) which clearly indicates some enhancement effect when part of the Co is replaced by Ni. Moreover, our previous studies indicated that the high HER and OER catalytic activity of non-precious metal doped N-carbon might originate from the formation of interfacial covalent M–N–C and M–O–C bonds which can provide additional active centers in the synthesized hybrids.[53, 54] Bond formation between inorganic nanocatalysts and the underlying carbon support could change the chemical bonding environment for carbon, oxygen, and metal atoms in the hybrid material, resulting in enhanced catalytic activity. Overall, the larger ΔE of 1.974 V for unsupported $Ni_{0.5}Co_{0.5}$ further confirms highly improved conductivity and charge transfer capability of N-carbon supported binary composites which are favorable for high HER and OER activity and stability.

Furthermore, the porous structure of prepared electrodes can enhance the catalysts contact area and the mass transport of electrolytes. As a consequence, favorable mass and charge transport can allow high utilization efficiency of active species for catalysis. It is reported that electrochemically active surface area (EASA) is directly proportional to a number of active sites which can be evaluated by the electrochemical double-layer capacitance (C_{dl}).[55] Fig. S13 (a-d) and S14 (a-d) show the representative cyclic voltammograms of binary Ni_xCo_{1-x}/NC and individual Ni/NC and Co/NC electrodes at different scan rates in a potential region of -0.8 to -0.75 V (ΔE = 50 mV). The CV exhibits a typical rectangular feature of an electrical double layer capacitor. In this potential region, charge transfer electrode reactions were considered to be negligible and the current is solely from the electrical double layer charging and discharging. The plot of current against potential scan rate has a linear relationship (Fig. S13e and S14e) and its slope is the double layer capacitance. The correlation of C_{dl} with the HER and OER overpotential to reach a current density of 10 mAcm^{-2} for various electrodes is presented in Fig. 6. It is clearly seen that the $Ni_{0.5}Co_{0.5}$/NC has the highest C_{dl} and lowest HER/OER overpotential, demonstrating its improved catalytic activity and facilitated reaction kinetics compared to the other prepared electrodes. Further, the direct growth of active materials on conductive copper foil can greatly enhance the electron transport and adhesion between electrocatalytically active species on substrates, promote the structural stability for long-term usage and avoid utilization of polymeric binders and extra conductive additives, consequently reducing the dead volume and undesirable interface in electrodes.[56-58] The enhancement in electrocatalytic activity of $Ni_{0.5}Co_{0.5}$/NC has long been noticed. Ni substitution is believed to improve Co/NC activity by either enlarging its active surface area (geometric effect) and/or by increasing its conductivity (electronic effect).[47]

Next, a proof-of-concept experiment was conducted to demonstrate the possibility of utilizing bifunctional $Ni_{0.5}Co_{0.5}$/NC for full water splitting using a two-electrode setup ($Ni_{0.5}Co_{0.5}$/NC‖ $Ni_{0.5}Co_{0.5}$/NC) in 1.0 M KOH. Other electrolyzers were prepared as controls using Pt/C as the cathode and IrO_2/C as the anode (Pt/C‖IrO_2) and cells using single Ni/NC and Co/NC, both as bifunctional electrodes (Ni/NC‖Ni/NC and Co/NC‖Co/NC) for comparison. As shown in Fig. 7a, $Ni_{0.5}Co_{0.5}$/NC needs 1.75 V to afford a 10 mAcm^{-2} water-splitting current. Although this voltage is larger than that for Pt/C‖IrO_2/C (1.71 V), it is smaller than those of individual Ni/NC‖Ni/NC and Co/NC‖Co/NC (1.93 and 1.88 V, respectively). The bifunctional activity of $Ni_{0.5}Co_{0.5}$/NC is also much lower than that of $NiCo_2O_4$NA/CC (1.98 V) and other reported commercial electrolyzers (1.8 V to 2.0 V).[59, 60] Additionally, the practical operation of the catalyst is examined by electrolysis at a fixed potential of 1.6 V over an extended period. As observed in Fig. 7b, the cell exhibits considerable stability over nearly five hours. This exceptional durability shows promise for practical applications of this catalyst over long term operation.

Conclusions

In summary, nickel-cobalt nanoparticles supported on porous nitrogen doped carbon thin films (Ni_xCo_{1-x}/NC) were fabricated via a two-step pulsed laser deposition technique under reaction in background gas (N_2 gas) at room temperature. The binary $Ni_{0.5}Co_{0.5}$/NC composite not only demonstrated efficient electrocatalytic activity and durability for HER but offered

This journal is © The Royal Society of Chemistry 20xx

Please do not adjust margins

impressive catalytic performance for OER in alkaline medium. The outstanding catalytic performance of the developed composites was strongly correlated to the homogeneous distribution of nickel-cobalt active sites and synergetic coupling interaction with the porous N-carbon framework. This earth-abundant composite could undoubtedly hold great promise for other practical applications in energy storage and conversion systems.

Acknowledgements

This work is financially supported by the Australian Research Council (ARC) through the Discovery Project programs (DP130104459, DP140104062, DP160104866). The authors acknowledge A. Facibeni for performing SEM images of the samples.

Notes and references

1. A. S. Arico, P. Bruce, B. Scrosati, J.-M. Tarascon and W. van Schalkwijk, *Nat. Mater.*, 2005, **4**, 366.
2. Y. Li, M. Gong, Y. Liang, J. Feng, J.-E. Kim, H. Wang, G. Hong, B. Zhang and H. Dai, *Nat. Commun.*, 2013, **4**, 1805.
3. Z. Peng, D. Jia, A. M. Al-Enizi, A. A. Elzatahry and G. Zheng, *Adv. Energy Mater.*, 2015, **5**, 1402031.
4. Y. Wang, T. Zhou, K. Jiang, P. Da, Z. Peng, J. Tang, B. Kong, W.-B. Cai, Z. Yang and G. Zheng, *Adv. Energy Mater.*, 2014, **4**, 1400696.
5. J. Luo, J.-H. Im, M. T. Mayer, M. Schreier, M. K. Nazeeruddin, N.-G. Park, S. D. Tilley, H. J. Fan and M. Grätzel, *Science*, 2014, **345**, 1593.
6. Y. Zheng, Y. Jiao, L. H. Li, T. Xing, Y. Chen, M. Jaroniec and S. Z. Qiao, *ACS Nano*, 2014, **8**, 5290.
7. T. Y. Ma, J. Ran, S. Dai, M. Jaroniec and S. Z. Qiao, *Angew. Chem. Int. Ed.*, 2015, **54**, 4646.
8. H. Xu, R. Q. Zhang, A. M. C. Ng, A. B. Djurišić, H. T. Chan, W. K. Chan and S. Y. Tong, *J. Phys. Chem. C,* 2011, **115**, 19710.
9. J. Shi, J. Hu, Y. Luo, X. Sun and A. M. Asiri, *Catal. Sci. Tech.*, 2015, **5**, 4954.
10. J. Lai, S. Li, F. Wu, M. Saqib, R. Luque and G. Xu, *Energy Environ. Sci.*, 2016, **9**, 1210-1214.
11. W. Zhou, J. Zhou, Y. Zhou, J. Lu, K. Zhou, L. Yang, Z. Tang, L. Li and S. Chen, *Chem. Mater.*, 2015, **27**, 2026.
12. L. Trotochaud, J. K. Ranney, K. N. Williams and S. W. Boettcher, *J. Am. Chem. Soc.* , 2012, **134**, 17253.
13. M. W. Louie and A. T. Bell, *J. Am. Chem. Soc.*, 2013, **135**, 12329.
14. P. D. Tran, S. Y. Chiam, P. P. Boix, Y. Ren, S. S. Pramana, J. Fize, V. Artero and J. Barber, *Energy Environ. Sci.*, 2013, **6**, 2452.
15. Y.-P. Zhu, Y.-P. Liu, T.-Z. Ren and Z.-Y. Yuan, *Adv. Funct. Mater.*, 2015, **25**, 7337.
16. J. Qi, W. Zhang, R. Xiang, K. Liu, H.-Y. Wang, M. Chen, Y. Han and R. Cao, *Adv. Sci.*, 2015, **2**, 1500199.
17. M. Carmo, D. L. Fritz, J. Mergel and D. Stolten, *Int. J. Hydrogen Energy*, 2013, **38**, 4901.
18. J. Ji, L. L. Zhang, H. Ji, Y. Li, X. Zhao, X. Bai, X. Fan, F. Zhang and R. S. Ruoff, *ACS Nano*, 2013, **7**, 6237.
19. P. Mazzolini, P. Gondoni, V. Russo, D. Chrastina, C. S. Casari and A. L. Bassi, *J. Phys. Chem. C* 2015, **119**, 6988.
20. R. Matarrese, I. Nova, A. L. Bassi, C. S. Casari and V. Russo, *Chemical Engineering Transactions*, 2014, **41**, 313.
21. P. Gondoni, P. Mazzolini, V. Russo, A. Petrozza, A. K. Srivastava, A. Li Bassi and C. S. Casari, *Sol. Energ. Mat. Sol. Cells*, 2014, **128**, 248.
22. C. S. Casari, S. Foglio, M. Passoni, F. Siviero, C. E. Bottani and A. Li Bassi, *Phys. Rev. B*, 2011, **84**, 155441.
23. D. Cattaneo, S. Foglio, C. S. Casari, A. Li Bassi, M. Passoni and C. E. Bottani, *Surf. Sci.*, 2007, **601**, 1892.
24. H. Kim, in *Pulsed Laser Deposition of Thin Films*, John Wiley & Sons, Inc., 2006, DOI: 10.1002/9780470052129.ch11, pp. 239-260.
25. B. Bayatsarmadi, Y. Zheng, C. S. Casari, V. Russo and S. Z. Qiao, *Chem. Commun.*, 2016, (Submitted for publication).
26. P. L. Walker, J. F. Rakszawski and A. F. Amington, in *Determination of Graphitic and Amorphous Carbon*, ASTM Bulletin, 1955, **208**, 52.
27. W. Yang, T.-P. Fellinger and M. Antonietti, *J. Am. Chem. Soc.* , 2011, **133**, 206.
28. T.-P. Fellinger, F. Hasché, P. Strasser and M. Antonietti, *J. Am. Chem. Soc.* , 2012, **134**, 4072.
29. R. Liu, D. Wu, X. Feng and K. Müllen, *Angew. Chem. Int. Ed.*, 2010, **122**, 2619.
30. B. S. Girgis, Y. M. Temerk, M. M. Gadelrab and I. D. Abdullah, *Carbon Science*, 2007, **8**, 95.
31. G. Zhang and X. W. Lou, *Adv. Mater.* , 2013, **25**, 976.
32. Y. He, L. Xu, Y. Zhai, A. Li and X. Chen, *Chem. Commun.*, 2015, **51**, 14768.
33. M. Caffio, B. Cortigiani, G. Rovida, A. Atrei and C. Giovanardi, *J. Phys. Chem. B*, 2004, **108**, 9919.
34. J. Deng, P. Ren, D. Deng and X. Bao, *Angew. Chem. Int. Ed.*, 2015, **54**, 2100.
35. J. Yang, H. Liu, W. N. Martens and R. L. Frost, *J. Phys. Chem. C*, 2010, **114**, 111.
36. H. Fei, J. Dong, M. J. Arellano-Jimenez, G. Ye, N. Dong Kim, E. L. G. Samuel, Z. Peng, Z. Zhu, F. Qin, J. Bao, M. J. Yacaman, P. M. Ajayan, D. Chen and J. M. Tour, *Nat. Commun.*, 2015, **6**, 9668.
37. A. Lu, Y. Chen, H. Li, A. Dowd, M. B. Cortie, Q. Xie, H. Guo, Q. Qi and D.-L. Peng, *Int. J. Hydrogen Energy*, 2014, **39**, 18919.
38. A. C. Ferrari and J. Robertson, *Phys. Rev. B*, 2000, **61**, 14095.
39. A. C. Ferrari and J. Robertson, *Phys. Rev. B*, 2001, **64**, 075414.
40. C. S. Casari, C. S. Giannuzzi and V. Russo, *Carbon*, 2016, **104**, 190.
41. C. S. Casari, M. Tommasini, R. R. Tykwinski and A. Milani, *Nanoscale*, 2016, **8**, 4414.
42. L. Ravagnan, F. Siviero, C. Lenardi, P. Piseri, E. Barborini, P. Milani, C. S. Casari, A. Li Bassi and C. E. Bottani, *Phys. Rev. Lett.*, 2002, **89**, 285506.
43. S. Bailey and F. King, in *Fine Chemicals through Heterogeneous Catalysis*, ed. H. v. B. R. A. Sheldon, John Wiley & Sons, 2008, ch. 8, p. 636.
44. Y. Li, W. Qiu, F. Qin, H. Fang, V. G. Hadjiev, D. Litvinov and J. Bao, *J. Phys. Chem. C*, 2016, **120**, 4511.
45. A. Jena, N. Munichandraiah and S. A. Shivashankar, *J. Power Sources*, 2013, **237**, 156.
46. C. C. L. McCrory, S. Jung, J. C. Peters and T. F. Jaramillo, *J. Am. Chem. Soc.* , 2013, **135**, 16977.
47. Y. Li, P. Hasin and Y. Wu, *Adv. Mater.* , 2010, **22**, 1926.
48. T.-W. Lin, C.-J. Liu and C.-S. Dai, *Appl. Catal., B: Environ.*, 2014, **154–155**, 213.
49. J. Xie, H. Zhang, S. Li, R. Wang, X. Sun, M. Zhou, J. Zhou, X. W. Lou and Y. Xie, *Adv. Mater.* , 2013, **25**, 5807.
50. T. Takashima, K. Hashimoto and R. Nakamura, *J. Am. Chem. Soc.* , 2012, **134**, 18153.
51. B. Chi, J. Li, Y. Han and Y. Chen, *Int. J. Hydrogen Energy*, 2004, **29**, 605.

Please do not adjust margins

Please do not adjust margins

52. E. B. Castro, S. G. Real and L. F. Pinheiro Dick, *Int. J. Hydrogen Energy*, 2004, **29**, 255.
53. B. Bayatsarmadi, Y. Zheng, Y. Tang, M. Jaroniec and S.-Z. Qiao, *Small*, 2016, **12**, 3703.
54. T. Y. Ma, S. Dai, M. Jaroniec and S. Z. Qiao, *J. Am. Chem. Soc.* , 2014, **136**, 13925.
55. C.-Z. Yuan, Y.-F. Jiang, Z. Wang, X. Xie, Z.-K. Yang, A. B. Yousaf and A.-W. Xu, *J. Mater. Chem. A*, 2016, **4**, 8155.
56. X. Liu, Z. Chang, L. Luo, T. Xu, X. Lei, J. Liu and X. Sun, *Chem. Mater.*, 2014, **26**, 1889.
57. D. U. Lee, J.-Y. Choi, K. Feng, H. W. Park and Z. Chen, *Adv. Energy Mater.*, 2014, **4**, 1301389.
58. X. Liu, Z. Chang, L. Luo, T. Xu, X. Lei, J. Liu and X. Sun, *ChemInform*, 2014, **26**, 1889.
59. D. Liu, Q. Lu, Y. Luo, X. Sun and A. M. Asiri, *Nanoscale*, 2015, **7**, 15122.
60. K. Zeng and D. Zhang, *Prog. Energy Combust. Sci.*, 2010, **36**, 307.

This journal is © The Royal Society of Chemistry 20xx

Please do not adjust margins